FERMILAB-PUB-24-0575-T

Testing the Neutrino Content of the Muon at Muon Colliders

Rodolfo Capdevilla,[1] **Francesco Garosi,**[2,3,4] **David Marzocca,**[4] **Bernd Stechauner**[5,6]

[1]*Particle Theory Department, Fermi National Accelerator Laboratory, Batavia, IL 60510, USA*
[2]*Max-Planck-Institute für Physik, Boltzmannstraße 8, 85748 Garching, Germany*
[3]*SISSA International School for Advanced Studies, Via Bonomea 265, 34136, Trieste, Italy*
[4]*INFN, Sezione di Trieste, SISSA, Via Bonomea 265, 34136, Trieste, Italy*
[5]*CERN, Espl. des Particules 1, 1211 Geneva 23, Switzerland*
[6]*TU Wien, Karlsplatz 13, 1040 Vienna, Austria*

Abstract: Collinear emission of W bosons off a high-energy muon induces a large muon-neutrino component among the Parton Distribution Functions (PDFs) of a muon. In this paper we study the phenomenology related to the ν_μ PDF at future high-energy muon colliders. We examine total rates and differential distributions of the $e\bar{\nu}_e$ and $W\gamma$ production processes, which receive a large, and often dominant, contribution from this PDF, allowing for a detailed experimental study. We then demonstrate that PDFs can have significant implications for the Higgs precision program envisioned at muon colliders. In particular, our results indicate that neutrino-initiated contributions constitute up to 10% (30%) corrections to the cross section for the production of a single Higgs via Z boson fusion at a 3 TeV (10 TeV) muon collider.

Contents

1 Introduction

The Standard Model (SM) of particle physics offers our best understanding of the physics of fundamental particles and their interactions. It provides a plethora of precise predictions that have been confirmed at particle accelerators over many decades, culminating with the discovery of the Higgs boson in 2012 by the Large Hadron Collider (LHC). Nevertheless, fundamental physics at multi-TeV energy scales remains relatively untested and the presence of physics beyond the SM remains an exciting possibility, well motivated by the instability of the electroweak scale under quantum fluctuations. Exploring this energy range is the main scope of the next generation of colliders, be it indirectly with very precise measurements of electroweak (EW) and Higgs processes or directly by reaching multi-TeV center-of-mass partonic energies in direct searches. A muon collider (MuC) offers the unique opportunity to explore both these avenues with the same machine [1–7] (see also [8–23]).

Independently of the possible presence of new physics, SM dynamics has never been observed at these large energies and it offers a large number of new phenomena to be studied both experimentally and theoretically. Specifically, at energies much larger than the EW scale the effects of EW masses become negligible and EW symmetry becomes effectively restored. The phenomena related to EW restoration are multiple and offer a very interesting physics program with assured deliverables for future high-energy colliders. They encompass effects such as the onset of large EW Sudakov double-logarithmic corrections [24–30], collinear emission of EW radiation [31], and EW PDFs [32–42]. While some of these effects are already relevant at the LHC and will become even more so at a more energetic

hadron collider, they play a central role in the physics of a MuC, since the effects of QCD interactions are suppressed by the non-colored nature of the muon.

The effects of initial-state radiation (ISR), that give rise to PDFs, are well known and have been widely studied at electron-positron colliders. The emission of copious amount of collinear photons [43–46] causes a reduction of the viable center of mass (CoM) energy for the collisions and an increase of the probability for gamma-gamma collisions. When the energy of the lepton increases and EW restoration becomes manifest, QED interactions must be substituted by the complete SM and the collinear emission of W and Z bosons becomes important. In this sense, a multi-TeV lepton collider becomes effectively a *gauge boson collider* [47, 48]. A peculiar feature of EW radiation, not present in the cases of QED or QCD, is that the valence lepton can transform into a neutrino via the emission of a collinear W boson, contributing to the neutrino component of the lepton's PDFs. Being dominated by the emission of soft W bosons, this process induces the neutrinos to typically carry a large fraction of the original lepton energy. The neutrino PDF thus grows at large momentum fractions $x \simeq 1$, where it dominates over the gauge bosons PDFs [39–41].

In this paper, we investigate several aspects of the phenomenology of muon neutrino PDFs at a future MuC. We start in Section 2 by reviewing the neutrino PDF and providing an approximate analytic expression to the full numerical result, which we take from Ref. [41]. In Section 3 we study two processes where the contribution from the neutrino PDF is dominant and therefore could offer a potential cross-check for theoretical predictions. Specifically, we focus on $\mu\bar{\mu} \to e\nu$ and $\mu\bar{\mu} \to W\gamma$, where μ ($\bar{\mu}$) represents the muon (anti-muon) beam, including its full parton content. We calculate total and differential rates to assess sensitivity to the contribution from the neutrino PDF in addition to the irreducible background from Vector Boson Fusion (VBF) as a function of the p_T and rapidity of the final-state particles.

The physics program for the MuC includes also high-precision measurements of the Higgs couplings to levels comparable to a Higgs factory [8–13]. The dominant process for Higgs production at a MuC is single-production, which proceeds via VBF. In Section 4, we quantify how much muon and neutrino PDFs can influence the dependence of the production cross section on the Higgs couplings to EW gauge bosons. This information is crucial for future multi-variable fits of Higgs couplings. We also quantify the impact of the muon neutrino PDF in associated HW production. Finally, we conclude in Section 5.

2 The muon neutrino PDF of a muon

When the transverse momentum of a splitting process in the initial-state radiation is much smaller than the typical energy of the subsequent hard scattering, i.e. in the collinear limit $p_T^{\rm ISR} \ll E_{\rm hard}$, then it is possible to factorize the splitting amplitude from the hard scattering one, up to small power corrections [49–51]. This results in the well known formalism of parton distribution functions, that can be used to describe the resummed multiple emission of collinear initial-state radiation: $f_i(x, Q^2)$ describes the probability of finding the parton i inside the original particle, carrying a longitudinal momentum fraction x and at a factorization scale Q. In the case of lepton colliders, PDFs can be derived analytically from first principles by solving differential DGLAP equations [52–54]. At leading order,

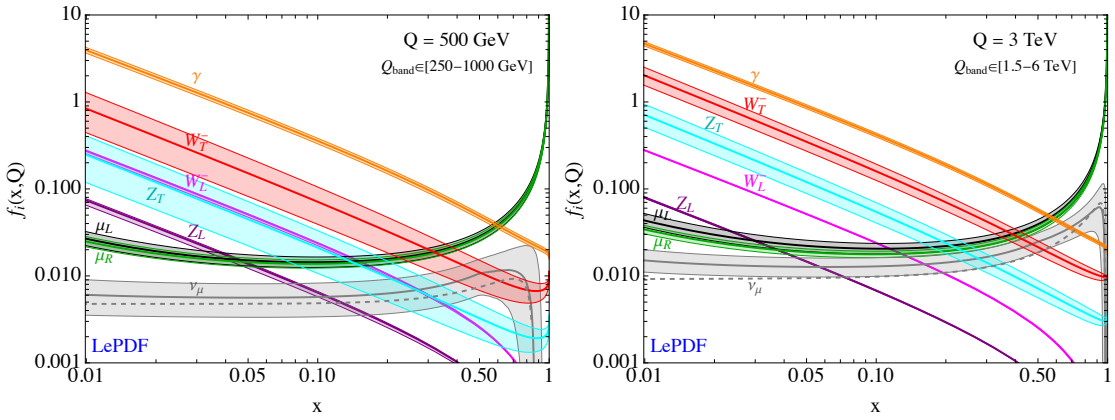

Figure 1. PDFs of a muon for a factorization scale $Q = 500\,\text{GeV}$ (left) and $Q = 3\,\text{TeV}$ (right), obtained with LePDFs [41]. The uncertainty bands correspond to the envelope obtained changing the factorization scale by a factor of 1/2 and 2. The dashed gray line is the result for the muon neutrino PDF obtained with the $\mathcal{O}(\alpha)$ expression in Eq. (2.1).

the boundary condition is set by imposing that at a factorization scale equal to the lepton mass, the only non-vanishing PDF is the one of the valence lepton itself and is a Dirac delta: $f^{(\alpha^0)}_{\ell_{\text{val}}}(x, m^2_{\ell_{\text{val}}}) = \delta(1-x)$.

At the lowest order in QED, $\mathcal{O}(\alpha)$, the only splitting process is $\ell^- \to \ell^-\gamma$, which generates a contribution to the photon PDF of the lepton, known at LO since a long time as the effective photon approximation [43–46], as well as a correction to the zeroth-order PDF of the valence lepton. This correction presents a soft IR divergence when the energy of the emitted photon goes to zero which, in the case of QED, is regulated by loop corrections to the electron self-energy, that must be included at the same order.

In the case of high-energy lepton colliders, specifically multi-TeV muon colliders, given the very large energy available in the hard scattering and the fact that electroweak radiation plays a leading role in the phenomenology (since leptons are not colored), it has been shown that complete EW interactions should be implemented in the PDFs and their evolution [31–42] In this work we use the recent implementation of LePDF [41], which resums at leading-logarithmic order the complete set of SM DGLAP equations. We report some examples of PDFs in Fig. 1, see also Refs. [39, 40] for other implementations.

Charged-current EW interaction has the peculiar property, not present in QED nor QCD, that it changes the fermion species: the analogous of the $\mu^- \to \mu^-\gamma$ splitting is $\mu^-_L \to \nu_\mu W^-$. As consequence, already at $\mathcal{O}(\alpha_2)$ a muon neutrino PDF is induced. While this splitting has the same IR soft divergence as in the QED case, EW loop corrections do not cancel it since the corresponding virtual correction only affects the muon PDF and not the neutrino one (see Sec. 3.2 of Ref. [41] for a simple demonstration). This is a violation of the Bloch-Nordsieck theorem [55], due to the initial and final states not being EW singlets. The IR divergence of the splitting therefore remains and is cutoff only by the W boson mass. A consequence of this fact is the presence of Sudakov double-logarithms, i.e. contributions to the PDFs that scale as $\alpha_2 \log^2 Q^2/m_W^2$ [24–30]. The soft IR divergence also implies that

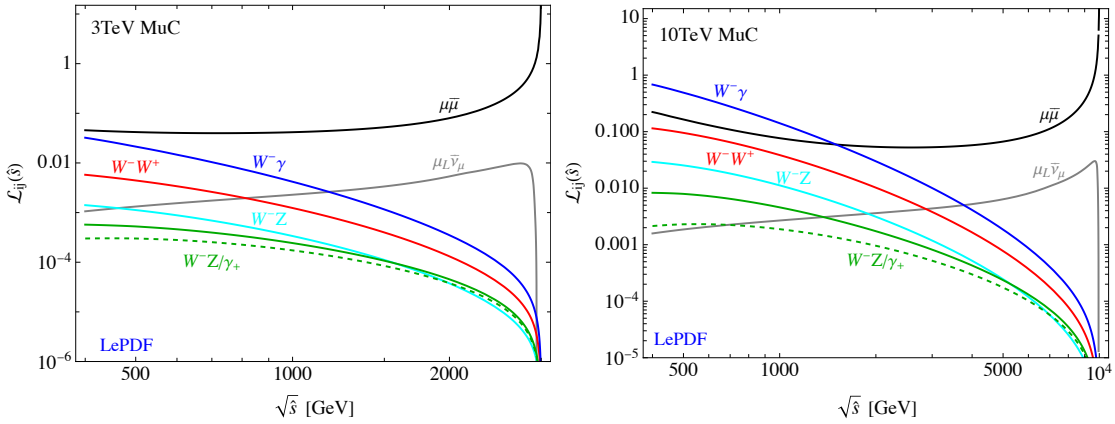

Figure 2. Some examples of parton luminosities for a 3 TeV (left) and 10 TeV (right) MuC. The factorization scale is chosen as $Q = \sqrt{\hat{s}}/2$. Unless written explicitly, different polarizations are summed. For the W^--Z/γ luminosity we sum over the W polarization and show with a solid (dashed) green line the result for the positive (negative) Z/γ helicity, in modulus.

most collinear gauge bosons are emitted with small energies and therefore we expect the muon neutrino PDF to increase when x nears 1. This features can indeed be observed in Fig. 1. The subsequent fall of the muon neutrino PDF very close to $x = 1$ is instead due to the infrared cutoff set by the W mass.

As shown in Ref. [41], by solving the EW DGLAP equations iteratively at $\mathcal{O}(\alpha_2)$ we can derive an approximate analytic expression for the neutrino PDF:

$$f_{\nu_\mu}^{(\alpha_2)}(x,Q^2) = \frac{\alpha_2(Q)}{8\pi}\,\theta\!\left(Q^2 - \frac{m_W^2}{(1-x)^2}\right)\left[\frac{1+x^2}{1-x}\left(\log\frac{Q^2+xm_W^2}{m_W^2} + \right.\right. \\ + \log\frac{(1-x)^2}{1+x(1-x)^2} + \frac{xm_W^2}{Q^2+xm_W^2} + \frac{1}{1+x(1-x)^2} - 1\Big) \\ \left. + \frac{2x^2(1-x)^2}{(1-x)(1+x(1-x)^2)}\,\frac{Q^2-m_W^2}{Q^2+xm_W^2}\right]\,, \tag{2.1}$$

where θ is the Heaviside step function that follows from the IR cutoff mentioned above. The last line is due to ultra-collinear emission of a longitudinal W boson from the muon. This analytic result is shown as a dashed gray line in Fig. 1, showing a good agreement with the full numerical result from LePDF. Further contributions to the neutrino PDF are expected at $\mathcal{O}(\alpha_2^2)$ mainly via the splitting $Z \to \bar{\nu}\nu$ and indeed we observe that the deviation grows at small x and for larger factorization scales, where the Z PDF is larger.

An estimate of the PDF uncertainties due to missing higher orders is typically obtained by varying the factorization scale. In Fig. 1 we show with colored bands the envelope, for each PDF, obtained by varying the factorization scale Q by a factor of 1/2 and 2 around the central value of 500 GeV (left) or 3 TeV (right). We see that these uncertainties are small for the photon, muon and the longitudinal polarization of EW bosons, while they are much larger for the transverse polarizations of W and Z, and for the muon neutrino. This can be understood as follows. The longitudinal W_L and Z_L PDFs receive the dominant contribution from ultra-collinear emission off the valence muon. Such terms have no logarithmic scaling

with Q and approach instead a constant value at large scales [31], hence the very small scale dependence. The different scale dependence between the photon and muon on the one hand, and W_T, Z_T, and muon neutrino on the other, is due to the fact that the former have a leading contribution from QED interactions starting from the m_μ scale, i.e. scaling as $\log Q^2/m_\mu^2$, while the latter evolve approximately as $\log Q^2/m_W^2$. For instance a variation of Q by a factor of 2 around 500 GeV gives a relative $\sim 8\%$ effect in the case of QED contributions, compared to a $\sim 38\%$ change for EW ones. These reduce to $\sim 7\%$ and $\sim 19\%$, respectively, around $Q = 3$TeV. It is clear that in order to obtain precise SM predictions such uncertainties should be reduced by deriving higher-order EW PDFs. Some discussions on possible extensions to higher order resummation can be found in Refs. [30, 38].

In Fig. 2 we show some examples of parton luminosities (see Eq. (A.5)), where for simplicity we sum over polarizations, except for W^--Z/γ, where we sum only over the W polarizations[1]. We fix $Q = \sqrt{\hat{s}}/2$ as factorization scale and do not report uncertainty bands, in order to not over-crowd the figure. It can be observed that for large invariant masses the $\mu^-\mu^+$ and $\mu_L^-\bar{\nu}_\mu$ luminosities dominate over the gauge bosons ones, as a consequence of the growth of both muon and neutrino PDFs for $x \to 1$.

3 Assessing the ν_μ PDF at muon colliders

In this Section, we investigate SM processes that are particularly sensitive to the neutrino PDF. Specifically, we focus on $\mu\bar{\mu} \to e^-\bar{\nu}_e$ and $\mu\bar{\mu} \to W^-\gamma$, where the contribution from the ν_μ PDF plays a leading role. These examples allow us to assess quantitatively the potential for testing experimentally the related SM predictions and could be used in the future to establish a proper treatment of EW-radiation effects in high-energy processes.

3.1 Single-electron production

The main process which could be used as a probe of the muon neutrino PDF is $\mu\bar{\mu} \to e^-\bar{\nu}_e$, where the partonic process we are interested in is

$$\mu^-\bar{\nu}_\mu \to e^-\bar{\nu}_e, \tag{3.1}$$

which proceeds via s-channel W exchange. We refer to this as the signal. The irreducible background arises via VBF:

$$\begin{aligned} W^-\gamma &\to e^-\bar{\nu}_e, \\ W^-Z &\to e^-\bar{\nu}_e. \end{aligned} \tag{3.2}$$

The Feynman diagrams for these processes are depicted in Fig. 3, where the upper left diagram corresponds to the signal and the others to the background. The calculation of the background cross section includes the effect of interference between the photon and transverse Z processes, which is then convoluted with the mixed Z/γ PDF [26, 31, 35, 41, 56].[2] We

[1] The two W^--$Z/\gamma_\pm$ luminosities have opposite sign and similar magnitude, giving an unphysical cancellation once they are summed.

[2] A dedicated study on the effects due to to the Z/γ PDF at MuC can be found in Ref. [56].

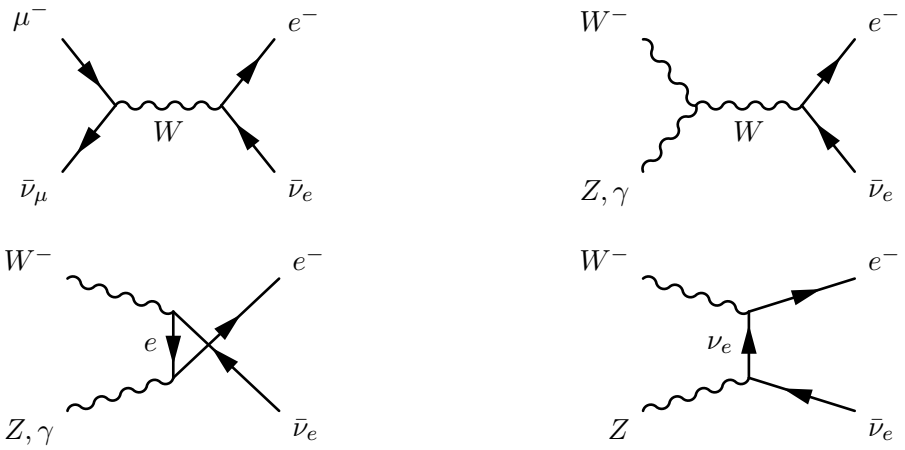

Figure 3. Leading partonic diagrams, in unitary gauge, contributing to $e^-\bar{\nu}_e$ production at a MuC.

neglect other background processes such as $e^-\bar{\nu}_e \to e^-\bar{\nu}_e$, $\tau^-\bar{\nu}_\tau \to e^-\bar{\nu}_e$, and $d_i\bar{u}_j \to e^-\bar{\nu}_e$, since their effects are further suppressed by small parton luminosities, see Ref. [41].

We can start to understand the relative weights of signal and background processes with simple estimates. The partonic cross sections of the two processes, for partonic invariant masses above the EW scale $\hat{s} \gg m_W$, follow the same scaling $\hat{\sigma}_{\mu\bar{\nu}} \sim \hat{\sigma}_{\rm VBF} \sim \alpha_{\rm EW}^2/\hat{s}$. The physical cross section is obtained by convoluting these with the corresponding parton luminosities in Fig. 2. Since the $\mu\bar{\nu}_\mu$ luminosity dominates over the VV ones at large invariant masses, we can expect that the signal will dominate the cross section in the high-energy region. This makes the $e^-\bar{\nu}_e$ process particularly sensitive to the neutrino PDF.

The physical triple differential cross sections for both signal and backgrounds are obtained by convoluting the partonic ones with the PDFs of the initial-state partons:[3]

$$\frac{d^3\sigma(\mu\bar{\mu} \to e^-\bar{\nu}_e + X)}{dy_e dy_\nu dp_T} = \sum_{i,j} f_i^\mu\left(x_1, \frac{\hat{s}}{4}\right) f_j^{\bar{\mu}}\left(x_2, \frac{\hat{s}}{4}\right)\left(\frac{2p_T\hat{s}}{s_0}\right)\frac{d\hat{\sigma}}{d\hat{t}}(ij \to e^-\bar{\nu}_e)(\hat{s}, \hat{t}) \ , \quad (3.3)$$

We refer to Appendix A for details and the expressions of the kinematical variables in terms of the final state's rapidities $y_{e,\nu}$ and p_T. Since the neutrino cannot be detected, we integrate over y_ν to obtain the double differential cross section in terms of y_e and p_T. We then bin these two variables to derive the total cross sections for both the signal and the background in each bin. Our results are shown in Fig. 4. The top-left panel displays the signal cross section (denoted by $\sigma_{\mu\nu}$), while the top-right panel shows the background cross section (denoted by $\sigma_{\rm bg}$). These cross sections correspond to a 3 TeV muon collider. We restrict the p_T of the electron to values greater than 500 GeV to ensure the validity of the collinear approximation for electroweak PDFs, where $m_{\rm EW} \ll E_{\rm hard} \sim p_T^e$. The rapidity is considered within the interval [-2, 2], motivated by the geometrical acceptance of the detector, ensuring

[3]The formula is exact when the two partons and the final states are all massless. The generalization to massive partons, which is the case for the background, is straightforward and we checked that differences are negligible in the kinematical regime where collinear factorization can be applied, i.e. $p_T \gg m_W$.

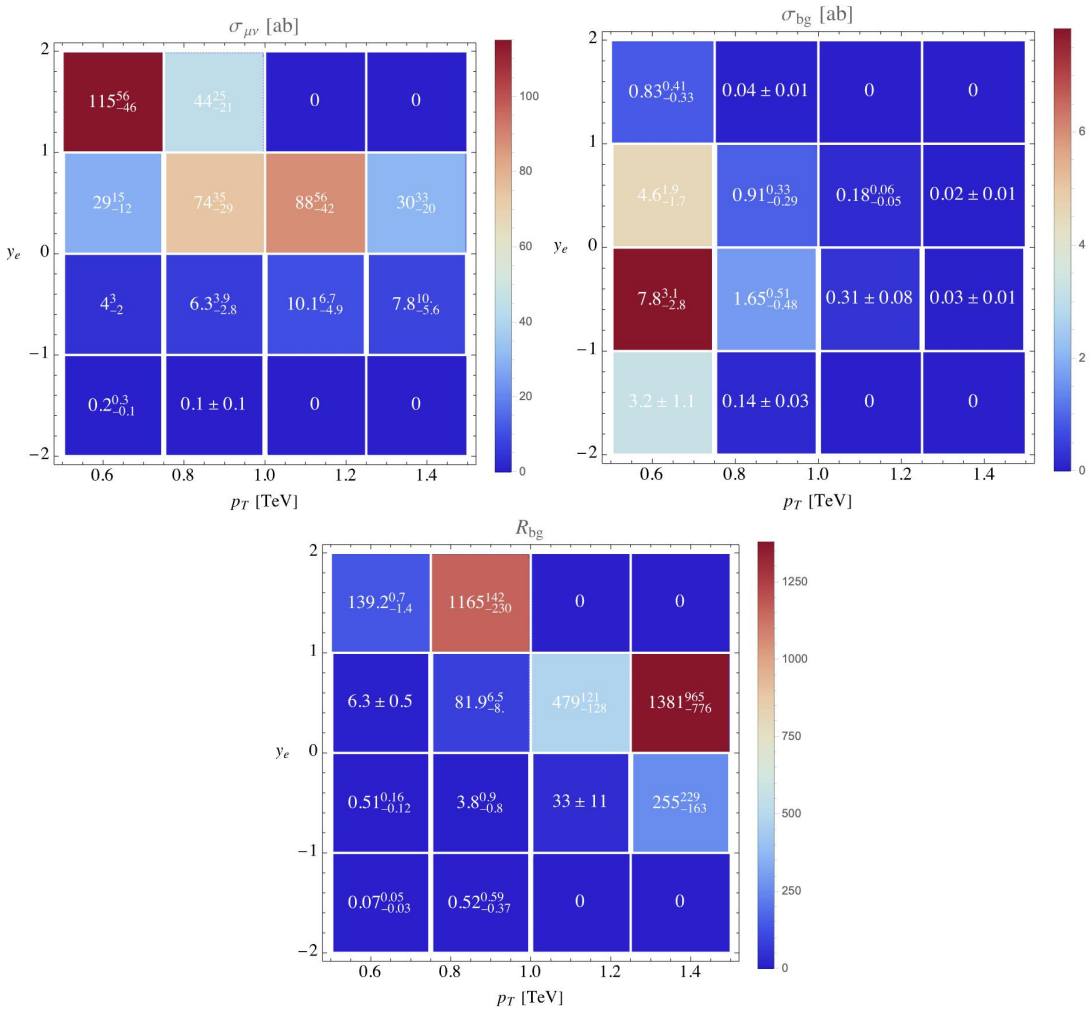

Figure 4. Top: Binned cross section for $\mu\bar{\mu} \to e^-\bar{\nu}_e$ at a 3 TeV Muon Collider, showing only the signal (left panel) or the background cross section (right panel). Bottom: Ratio of the signal cross section over the the VBF background.

we focus on events away from the forward nozzles [57], which are generally cleaner and less affected by beam-induced backgrounds [58].

Comparing the two top panels in Fig. 4, we observe a significant difference between the signal and background distributions as a function of p_T. At relatively low $p_T \in (500, 750)$ GeV, the signal is largely forward, with its rapidity distribution peaking in the most forward bin ($y_e > 1$) and rapidly decreasing at lower rapidities ($y_e < 1$). In contrast, the background distribution peaks in the near-central region ($-1 < y_e < 0$) and is highly suppressed in the most forward rapidity bin. This behavior can be understood because the signal originates from a purely left-handed scattering amplitude, where the left-handed nature of the neutrino forces the final state to favor a helicity configuration that drives the electron forward. On the other hand, the background consists of vector bosons, whose helicity states can be either transverse or longitudinal. These states can add up to several helicity configuration, which

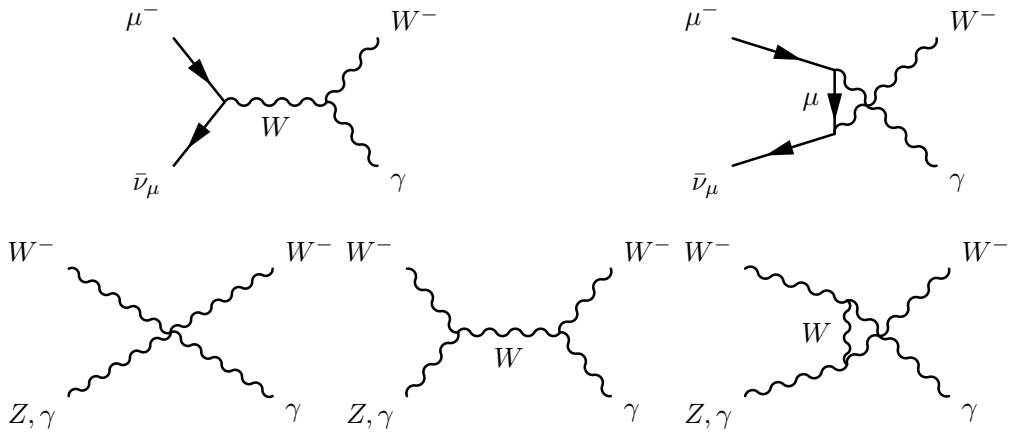

Figure 5. Leading partonic diagrams contributing to $W\gamma$ production at a MuC, in unitary gauge, for both the signal (upper line) and the background (lower line).

contribute in different amounts to the total amplitude.

As the p_T of the final state electron increases, both the signal and background distributions shift towards more central rapidities, due to kinematical constraints, see Eq. (A.4). However, the background is significantly suppressed compared to the signal. This behavior arises from the fundamental difference between the PDFs of gauge bosons, that are peaked at small momentum fractions of the muon beam, and the ones of the muon and the muon neutrino, which instead are peaked at high momentum fractions, as discussed in Section 2 (see Fig. 1). To quantify the impact of neutrino PDF on this process, we define the following ratio

$$R_{\rm bg}^{e\nu} = \frac{\sigma_{\mu\nu}^{e\nu}}{\sigma_{\rm bg}^{e\nu}}, \tag{3.4}$$

where the label $e\nu$ is simply to specify the final state. This ratio can be used to establish the ideal place to look for neutrino PDF contributions, i.e. in bins where both the R ratios and the cross section are big enough. The results are shown in the bottom panel of Fig. 4. In conclusion, the contribution of the neutrino PDF to single-electron production is maximized at large p_T and, for intermediate p_T values, in the forward regions of the rapidity distribution.

3.2 $W\gamma$ production

The associated production of a photon and a W, $\mu\bar{\mu} \to W^-\gamma$, follows the same lines as the single-electron production: at the parton level we have a neutrino-induced signal while the background proceeds via vector boson fusion:

$$\begin{aligned} &\mu^-\bar{\nu}_\mu \to W^-\gamma, \\ &W^-\gamma \to W^-\gamma, \\ &W^-Z \to W^-\gamma. \end{aligned} \tag{3.5}$$

The relevant Feynman diagrams are shown in Fig. 5. As for single-electron production, we neglect background processes induced by initial-state electrons, taus, and quarks due to

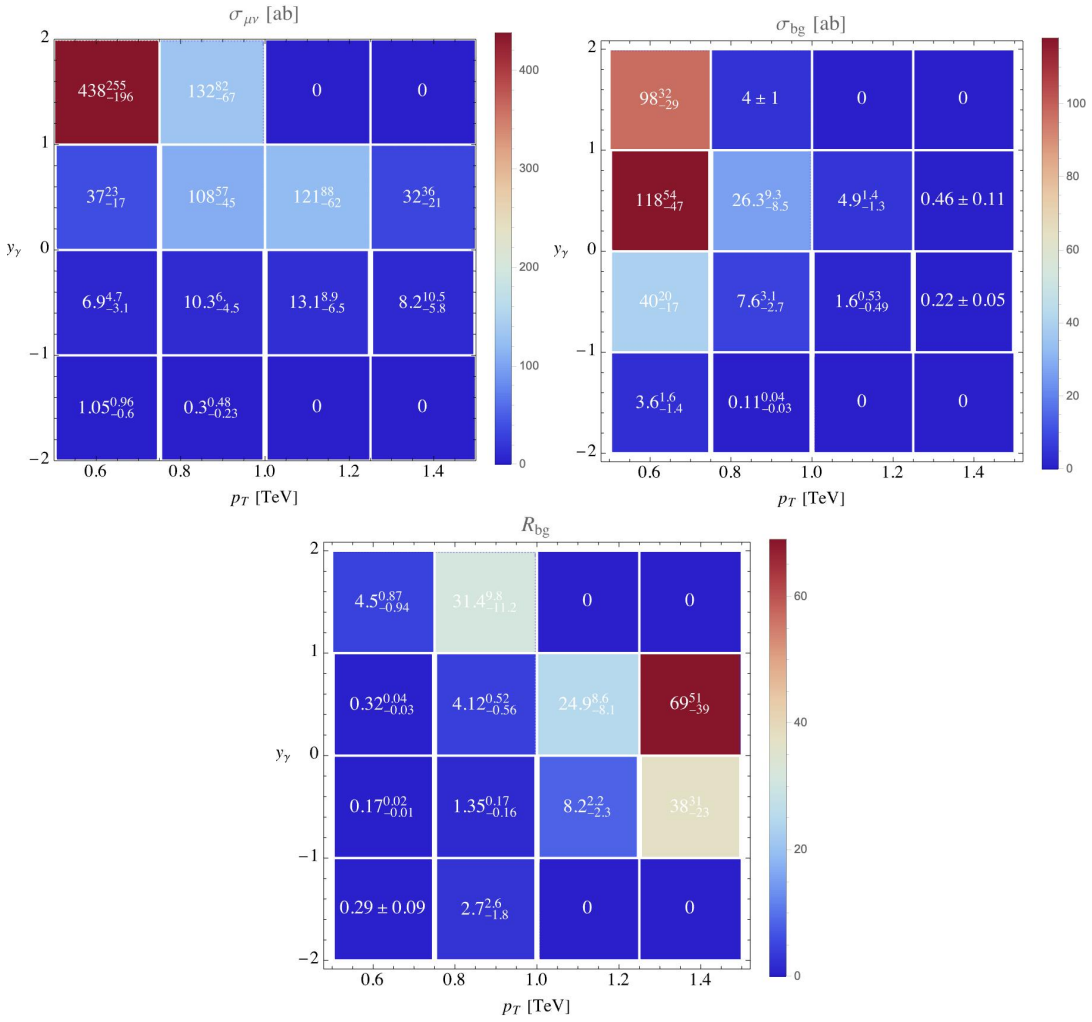

Figure 6. Top: Binned cross section for $\mu\bar{\mu} \to W^-\gamma$ at a 3 TeV Muon Collider, showing only the signal (left panel) or the background (right panel). Bottom: Ratio of the signal cross section over the VBF background.

the suppression of parton luminosity. It is worth noting that this process is less sensitive to the neutrino PDF, as the background partonic cross section $\hat{\sigma}_{\rm VBF}$ remains constant at high energies, whereas $\hat{\sigma}_{\mu\bar{\nu}} \sim \alpha^2_{\rm EW}/\hat{s}$, as previously discussed.

Since the rapidity of the W boson is also measurable, one can, in principle, study triple-differential distributions for this process using the formula in Eq. (A.1). Factorization holds when the invariant mass of the hard scattering is much larger than the electroweak scale, allowing us to neglect the particle masses in our analysis. For simplicity, we perform a similar analysis as in Section 3.1, focusing on double-differential distributions in the transverse momentum (p_T) and the rapidity (y_γ) of the final-state photon.[4] Our results for the signal ($\sigma_{\mu\nu}$) and background ($\sigma_{\rm bg}$) are shown in the top-left and top-right panels of

[4]We choose to use the photon rapidity being it easier to measure, without the need to reconstruct the W from the decay products.

Fig. 6, respectively. The signal is concentrated in the most forward rapidity region when p_T is small, similar to the single-electron case. This behavior arises from the maximally broken parity of the initial state fermions. In contrast to the single-electron case, however, the background is also strongly forward in the low-p_T region. Nevertheless, as p_T increases, the signal becomes more central, and the background is significantly suppressed, enabling a clearer measurement of the neutrino PDF contribution to $W\gamma$ production.

Finally, similar to the single-electron case, we define the ratio

$$R_{\rm bg}^{W\gamma} = \frac{\sigma_{\mu\nu}^{W\gamma}}{\sigma_{\rm bg}^{W\gamma}}. \tag{3.6}$$

The results are shown in the bottom panel of Fig. 6, which depict a very similar behavior to that of single-electron production.

An interesting aspect of the $W\gamma$ process, unlike the single-electron case, is that the momenta of both final-state particles can be reconstructed, allowing us to determine the center of mass of the $W\gamma$ system. This offers two key advantages: (1) we can compute the angular distribution of the W boson relative to the boost of the system ($\cos\theta$), which reveals the so-called Radiation Amplitude Zero (RAZ) [59–61].[5] For the $\mu\nu \to W^-\gamma$ process, the RAZ appears in the most forward region of the $\cos\theta$ distribution.[6] (2) By reconstructing the center of mass energy, we can study how the $W\gamma$ cross section evolves with $\sqrt{\hat{s}}$. As $\sqrt{\hat{s}}$ increases, the background diminishes while the signal strengthens, mimicking the behavior of the luminosity functions in Fig. 2, as we already saw by quantifying how the neutrino PDF contribution dominates at high p_T.

3.3 Comparison between PDF and fixed-order approaches

As discussed above, employing PDFs to describe ISR gives a good approximation, and allows to resum leading logarithms, if the emitted radiation is collinear, that is its p_T is much smaller than the typical energy scale involved in the hard scattering. The main disadvantages of this approach is that the collinear radiation is integrated over, so cannot be described in a differential way, and that power-like corrections are neglected.

An alternative approach is to perform a fixed-order calculation, where the full process is described, including ISR. On the one hand, in this way the collinear radiation is fully described and can be used as an experimental handle to select interesting events, on the other hand the possibly large double logarithms are not resummed and therefore it might suffer from large uncertainties in the high-energy regime [70]. Our goal in this Section is to compare the two approaches, at the lowest order, in the case of the simple process of $e^-\bar{\nu}_e$ production. Specifically, in the following we focus only on the $\mu^-\bar{\nu}_\mu$ fusion contribution, neglecting VBF. As shown in Section 3.1, the former is by far the dominant contribution in the hard region of large electron p_T^e.

At leading order, single-electron production at muon colliders proceeds via $\mu^-\mu^+ \to e^-\bar{\nu}_e W^+$. The leading order Feynman diagrams are shown in Fig. 7. For the purpose of the

[5] The RAZ was first discovered in [62], observed at the Tevatron [63], and recently measured at the LHC [64–67]. This feature of multi-boson scattering enhances sensitivity to new physics searches [68].

[6] A detailed analysis of the RAZ and its detectability at multi-TeV MuC will be explored elsewhere [69].

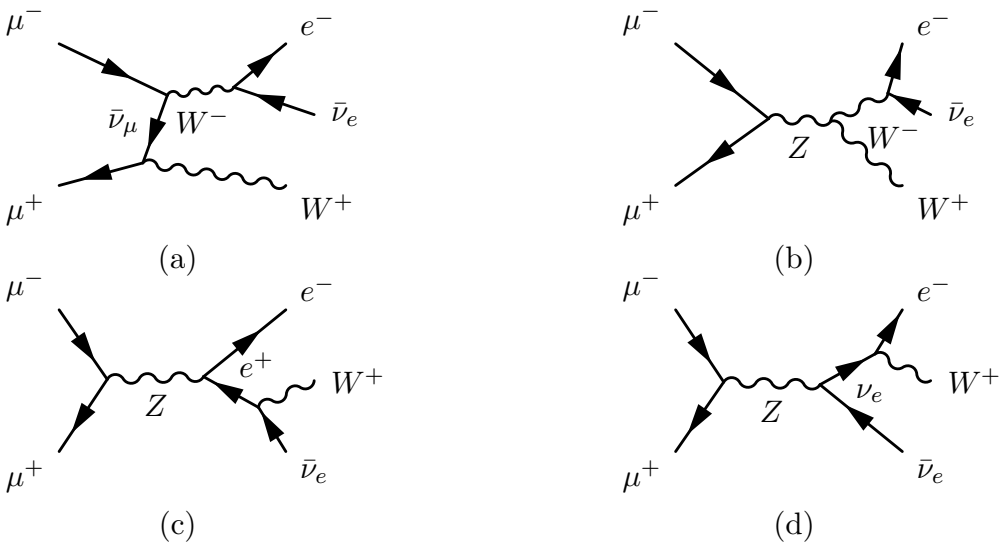

Figure 7. Leading-order Feynman diagrams for $\mu^-\mu^+ \to e^-\bar{\nu}_e W^+$.

comparison with the PDF approach we are interested in the region where the final-state W is collinear and is emitted by the initial μ^+, diagram (a). This process however receives two other contributions, that should be removed with appropriate cuts to isolate the collinear W emission. The first arises from on-shell W^-W^+ pair-production, with W^- decaying to electron-neutrino (Fig. 7-(b)). This contribution is characterized by an invariant mass of the electron-neutrino pair close to the W mass and central Ws. The second is through production of e^-e^+ or $\nu_e\bar{\nu}_e$ via neutral current, with subsequent emission, like final state radiation (FSR), of a W^+ boson from either the e^+ or the ν_e (Fig. 7-(c,d)). These W^+ are typically emitted collinearly from the lepton and with small energies, due to the infrared singularity of the splitting function.

We study the cross section in different bins of p_T^e. For the PDF approach at a 3 TeV MuC we can use the result reported in Fig. 4, integrating over the electron rapidity y_e between -2 and 2. The corresponding cross section in p_T^e bins, for both the 3 TeV and 10 TeV MuC are shown as a blue line in Fig. 8, with the blue band representing the factorization scale uncertainty. To evaluate the fixed-order cross section we generate with `MadGraph5_aMC` [71] $\mu^-\mu^+ \to e^-\bar{\nu}_e W^+$ events at leading order with 3 and 10 TeV of total invariant mass. Since our only goal is to compare the two theoretical approaches, in the following we pretend that the four momenta of all final-state particles can be fully reconstructed, including the neutrino. At generation level we impose the following cuts, that we label as (1):

$$\begin{aligned}(1)_{3\text{TeV}} &: |y_e| < 2\ , \quad p_T^e > 500\,\text{GeV}\ , \quad p_T^\nu > 500\,\text{GeV}\ , \quad M(e,\nu_e) > 200\,\text{GeV}\ , \\ (1)_{10\text{TeV}} &: |y_e| < 2\ , \quad p_T^e > 1\,\text{TeV}\ , \quad p_T^\nu > 1\,\text{TeV}\ , \quad M(e,\nu_e) > 500\,\text{GeV}\ .\end{aligned} \tag{3.7}$$

The former two cuts are the same as the ones used in Fig. 4 while the latter two, that are automatically satisfied in the PDF approach (since in that case $p_T^\nu = p_T^e$ and $M(e,\nu_e) = 2p_T \cosh\left((y_e - y_\nu)/2\right) > 2p_T$), are used to remove the otherwise overwhelming contribution

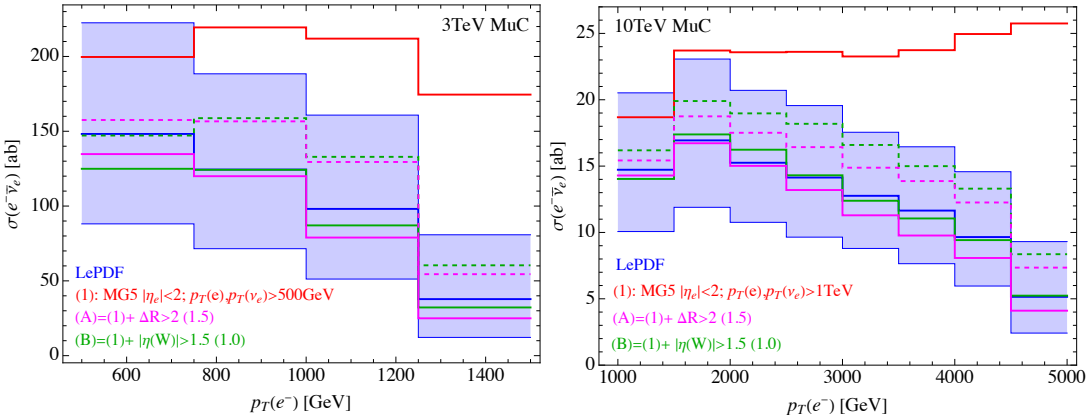

Figure 8. Comparison between PDF and fixed-order results for $e^-\bar{\nu}_e$ production at a 3 TeV (left) and 10 TeV (right) MuC, with subsequent cuts imposed on the leading-order events generated with `MadGraph5_aMC`. Dashed magenta and green lines correspond to the cuts shown in parentheses.

from on-shell WW production and to ensure the hardness of the $e^-\bar{\nu}_e$ system. We note that at this point almost all events have $M(e,\nu_e) \gtrsim 1\,(2)$ TeV for the 3 (10) TeV MuC and $\Delta\phi(e,\nu_e) \approx \pi$. The resulting cross section in bins of p_T^e is shown as a red line in Fig. 8. One can notice a large mismatch with the result obtained from the PDF approach, that does not even improve with large p_T^e. This is due to the W^+ emitted as FSR from final-state leptons, i.e. diagrams (c,d) in Fig. 7.

To remove this contribution and ensure that only the collinear W region is selected, we present two alternatives. The first, that we denominate as (A), is to impose an isolation criteria on both the electron and the neutrino, requiring

$$\text{(A)}: \quad \Delta R(i,j) > 2 \text{ or } 1.5\ , \tag{3.8}$$

for all three final state particles $i,j = e^-, \bar{\nu}_e, W^+$, and $\Delta R = \sqrt{(\Delta\eta)^2 + (\Delta\phi)^2}$. While this is automatically satisfied for the electron-neutrino pair, given they have $\Delta\phi(e,\nu_e) \approx \pi$, this cut ensures that the W^+ is not collinear with the final-state leptons. The electron-p_T distribution for this case is shown with magenta lines (respectively solid and dashed for the two values of the cut) in Fig. 8, and shows a good agreement with the PDF result.

The second alternative, denominated as (B), is to impose a mild cut on the W pseudo-rapidity,

$$\text{(B)}: \quad |\eta_W| > 1.5 \text{ or } 1.0\ . \tag{3.9}$$

Also this cut brings the fixed-order result in good agreement with the PDF one for both cut values, as shown with the green lines in Fig. 8 (respectively solid and dashed for the two cuts).

The p_T distribution of the W boson, normalized to 1, for each stage of the cuts described above is shown in Fig. 9 and shows how the collinear condition is well satisfied once the cuts (A) or (B) are applied.

These results clearly demonstrate that the cuts used are effective in isolating the collinear W emission and that the fixed-order calculations agree with the resummed predictions

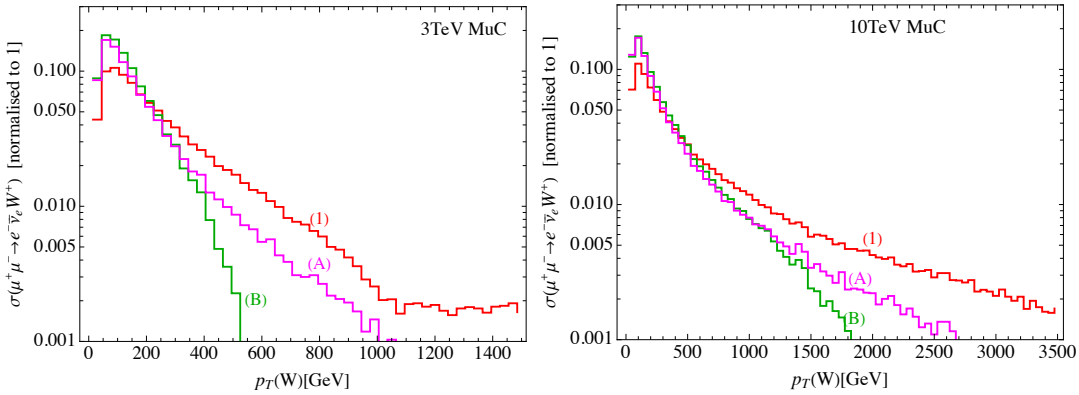

Figure 9. Normalized p_T distribution of the W boson for the various cut stages for the 3 and 10 TeV muon colliders.

obtained from the PDF approach within the scale uncertainties. However, there is a notable issue in this comparison: both cut types (A) and (B) are applied specifically to the W boson, which contrasts with the PDF approach, where the treatment of collinear radiation is inclusive. This difference in methodology may lead to discrepancies when comparing results between the two approaches. An indication of such discrepancies is presented by considering the difference between the solid and dashed lines, which corresponds to the two different values used in the cuts in (A) and (B). While the cuts we use are likely broad enough to approximate inclusivity, a more rigorous comparison would require applying identical cuts to both the fixed-order and resummed approaches. This challenge highlights a broader issue in the treatment of electroweak radiation at high-energy muon colliders, a topic that extends beyond the scope of our current study.

4 Impact on Higgs physics

The proposed muon colliders have the capability to reach both very high energies and luminosities. This, combined with the large parton luminosities of vector boson initial states, implies that such a collider could also function as a Higgs factory [2, 3, 5–7]. The relatively large cross sections, compared to an electron collider, combined with a clean environment, compared to a hadron collider, provide excellent prospects. Specifically, it has been shown that a 3 TeV MuC could reach a $\mathcal{O}(1\%)$ precision on several Higgs couplings, while a 10 TeV MuC could improve this down to $\mathcal{O}(0.1\%)$ [9, 11, 13]. At this level of precision it will be crucial to provide accurate SM predictions.

In a multi-TeV MuC, single-Higgs production via VBF is the most relevant channel for Higgs boson production. If ISR is neglected, only processes involving initial-state $\mu^-\mu^+$ interactions are considered. The dominant contribution arises from the charged current (CC) channel, $\mu^-\mu^+ \to \nu_\mu\bar{\nu}_\mu H$, followed by the neutral current (NC) channel, $\mu^-\mu^+ \to \mu^-\mu^+ H$, which is approximately an order of magnitude smaller in cross section:

$$\begin{aligned}\sigma_{(\text{no ISR})}(\mu^-\mu^+ \to \nu_\mu\bar{\nu}_\mu H)(s) &\approx 498\,\text{fb}|_{\sqrt{s}=3\,\text{TeV}} \;, \quad 843\,\text{fb}|_{\sqrt{s}=10\,\text{TeV}} \;, \\ \sigma_{(\text{no ISR})}(\mu^-\mu^+ \to \mu^-\mu^+ H)(s) &\approx 50.8\,\text{fb}|_{\sqrt{s}=3\,\text{TeV}} \;, \quad 87.4\,\text{fb}|_{\sqrt{s}=10\,\text{TeV}} \;.\end{aligned} \tag{4.1}$$

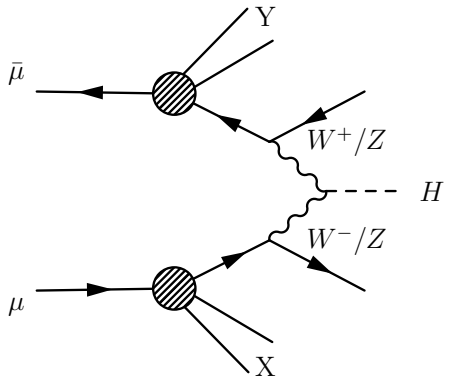

Figure 10. In the lepton parton model, the initial state leptons $(\mu^+, \mu^-, \nu_\mu, \bar{\nu}_\mu)$ in the hard process are emitted from collinear splittings of the initial muon or anti-muon beams. The possible partonic initial and final states are listed in Table 1.

The final state fermions (muons or neutrinos) are highly collinear, making it difficult to distinguish experimentally the two processes. Without a forward detector to disentangle these two processes, the MuC will enable measurement of the WWH and ZZH couplings with precision of 0.7% and 0.9%, respectively [8, 9, 11]. Tagging forward muons in the Z-fusion channel would allow model-independent determinations of the Higgs invisible branching ratio [10]. This forward tagger would also resolve the WWH/ZZH degeneracy, improving the precision of these couplings down to 0.3% [11, 13].[7]

In this context, the PDFs of a muon present two new effects. The first one is a change to the energy distribution of the initial $\mu^\pm$ states, mainly via the emission of collinear photons that go undetected (or are not tagged). In terms of PDF, this corresponds to the fact that, once collinear emissions are considered the muon PDF is not anymore a Dirac delta but develops a tail for smaller x values, see Fig. 1. Since the event rates for the processes in Eq. (4.1) increase with the center-of-mass energy, including the muon PDF shifts some events to lower invariant masses and therefore it has a negative impact on the cross sections. The second effect is due to collinear emission of W bosons from the initial muon beam which, as we discussed already, generates a muon neutrino PDF. We should therefore also consider processes with muon neutrinos in the initial state, which of course generate positive contributions to the total cross section. In Fig. 10 we show a schematic Feynman diagram for single-Higgs production, where the partonic initial-state leptons arise from the collinear splitting (shaded circles) off the initial muon and anti-muon beams. In the picture, X and Y represent collinear radiation.

In an exclusive approach, tagging this collinear radiation (mostly photons and EW gauge bosons) and a forward muon detector could offer experimental handles to disentangle

[7] Achieving these precision levels requires meeting certain experimental targets, as outlined in [12]. These include energy resolutions of 0.4% for muons, 3% for photons, and 15% for jets, tagging efficiencies of 60% for b-tagging and 20% for c-mistagging, and timing resolutions of 30-60 ps for the vertex detector and 100 ps for calorimeters. These targets are comparable to those achievable at the LHC and envisioned for the HL-LHC [72].

Partonic process	Channel	$\sigma(3\,\text{TeV})$ [fb]	$\sigma(10\,\text{TeV})$ [fb]
$\mu^-\mu^+ \to \nu_\mu \bar{\nu}_\mu H$	CC	$480.3^{+0.8}_{-0.7}$	$820.9^{+0.6}_{-0.2}$
$\mu^-\mu^+ \to \mu^-\mu^+ H$	NC	$47.7^{+0.6}_{-0.8}$	$80.5^{+1.5}_{-1.7}$
$\mu^-\bar{\nu}_\mu \to \mu^-\bar{\nu}_\mu H$	NC	$2.4^{+1.6}_{-1.2}$	10^{+4}_{-3}
$\nu_\mu\bar{\nu}_\mu \to \mu^-\mu^+ H$	CC	$0.19^{+0.45}_{-0.15}$	$2.4^{+3.0}_{-1.5}$
$\nu_\mu\bar{\nu}_\mu \to \nu_\mu\bar{\nu}_\mu H$	NC	$0.08^{+0.17}_{-0.06}$	$1^{+1.2}_{-0.6}$

Table 1. Cross sections at 3 TeV and 10 TeV muon colliders are divided according to the main partonic processes contributing to single Higgs production. The particles in the initial state are the partons involved in the hard scattering.

the various contributions, in which case one should employ fixed-order calculations to derive predictions. This strategy would however be heavily affected by the relatively restrictive acceptance of the detector in the forward regions. On the other hand, if one is inclusive on possible collinear EW radiation then the PDF approach is more suitable since it allows to resum all possible collinear emission of EW radiation and therefore also a resummation of the leading logarithms. Which approach to use depends on the specific goals of the analysis.

Since the muon neutrino PDF is always much smaller than the muon one, see Fig. 1, we expect that processes initiated by $\mu^-\mu^+$ dominate, followed by those induced by $\mu^-\bar{\nu}_\mu$ and $\nu_\mu\mu^+$, while the ones induced by $\nu_\mu\bar{\nu}_\mu$ will be doubly suppressed. This is confirmed by our numerical results, which include the effects of PDFs by convoluting the partonic total cross sections for single-Higgs production with the corresponding PDF pairs, as in Eq. (A.7). Our total cross sections for each channel are shown in Table 1, for a collider invariant mass of either 3 or 10 TeV. Here we consider only the dominant processes, i.e. with a muon (anti-muon) or a muon neutrino (anti-neutrino) as partons from the muon (anti-muon) beam, see Appendix B for all the possible processes contributing. We also report a theory uncertainty obtained by varying the PDF factorization scales, as discussed in Section 2. We can derive some significant conclusions from this table. Without ISR, tagging two forward muons could single out the neutral current contribution to single-Higgs production, i.e. the ZZH coupling. However, in the presence of collinear EW radiation, that might go undetected, the table shows that at a 10 TeV MuC this final state has a 3% contamination from the CC process $\nu_\mu\bar{\nu}_\mu \to \mu^+\mu^- H$, proportional to the WWH coupling instead. Furthermore, we argue that, in order to achieve sub-percent level precision in the determination of WWH and ZZH couplings, one needs to include the processes where only one forward muon is tagged. At a 10 TeV MuC this contribution is sizeable, as we can see from the third row of Table 1, where the cross section of $\mu^-\bar{\nu}_\mu \to \mu^-\bar{\nu}_\mu H$, plus the charge-conjugate process $\nu_\mu\mu^+ \to \nu_\mu\mu^+ H$, is about 25% of the other NC process $\mu^-\mu^+ \to \mu^-\mu^+ H$.

Cross sections [fb]	No PDFs	Only μ PDF	Both μ and ν_μ PDF
$\sigma^{3\text{TeV}}_{\kappa_W^2}$	498	480 (-3.6%)	480 (+0.04%)
$\sigma^{3\text{TeV}}_{\kappa_Z^2}$	50.8	47.7 (-6.1%)	52.6 (+10%)
$\sigma^{10\text{TeV}}_{\kappa_W^2}$	842	821 (-2.6%)	823 (+0.3%)
$\sigma^{10\text{TeV}}_{\kappa_Z^2}$	87.4	80.5 (-7.9%)	102 (+27%)

Table 2. Coefficients of κ_W^2 and κ_Z^2 in single-Higgs production cross sections at 3 and 10 TeV muon colliders, in fb. The second column shows the result obtained without considering ISR effects. The third column includes the muon PDF while the fourth column also adds the muon neutrino PDF. In parenthesis we show the relative change from the previous column. For simplicity we do not report here scale uncertainties, which can be seen in Table 1.

When using such Higgs production processes to set constraints on Higgs couplings, a framework commonly employed is the one of kappa-factors. In our case it corresponds to multiplying the tree-level Higgs coupling to Z and W bosons by a κ_Z and κ_W factor, respectively. The SM prediction is recovered, by definition, for $\kappa_Z = \kappa_W = 1$. Using this framework we can put together the various contributions to the single Higgs production cross section for 3 and 10 TeV muon colliders. The results are shown in Table 2, where we separate the coefficients multiplying κ_W^2 and κ_Z^2:

$$\sigma^{\text{N TeV}}_{\mu\bar{\mu}\to H+X} = \sigma^{\text{N TeV}}_{\kappa_W^2}\kappa_W^2 + \sigma^{\text{N TeV}}_{\kappa_Z^2}\kappa_Z^2 \ , \tag{4.2}$$

where $\sigma^{\text{N TeV}}_{\kappa_W^2}$ includes all those processes where the Higgs is produced via W boson fusion i.e. those labeled CC in Table 1, whereas $\sigma^{\text{N TeV}}_{\kappa_Z^2}$ corresponds to Z boson fusion (NC) processes. We observe that the coefficient of κ_W^2 is affected mainly by the muon PDF. The effect at a 3 (10) TeV MuC is to decrease the cross section by 3.6% (2.6%) with respect to the leading-order no-ISR result (compare the second and third columns in Table 2 for $\sigma^{\text{N TeV}}_{\kappa_W^2}$). The neutrino PDF instead has negligible impact, since the only contribution requires neutrino PDFs in both initial legs, amounting to a large suppression (compare the second and third columns in Table 2 for $\sigma^{\text{N TeV}}_{\kappa_W^2}$). In case of κ_Z^2 we see a similar depletion due to the muon PDF, now of about 6.1% (7.9%) at a 3 (10) TeV MuC. Initial-state muon neutrinos, mostly via $\mu^-\bar{\nu}_\mu \to \mu^-\bar{\nu}_\mu H$ plus the conjugate process, give a large and positive contribution of about 10% (27%) at a 3 (10) TeV MuC.

We can conclude that a proper inclusion of both ISR from the valence muon and the contributions arising from muon neutrino PDF should be included in the Standard Model predictions for single-Higgs production, since the corresponding effects are much larger than the expected statistical precision attainable in these measurements, both in the case where final state muons are tagged and if they are not.

In order of cross section, the third most common Higgs production channel at a 3-10 TeV MuC is associated WH production. While the dominant contribution for this process comes from VBF, a small contribution is induced by the neutrino PDF via $\mu^-\bar{\nu}_\mu \to W^* \to W^-H$. For a more detailed discussion we refer to the results presented in Ref.[56], where the $\mu\bar{\mu} \to W^-H$ cross section was computed at leading order using LePDF with cuts $|y_W| < 2$,

$|y_H| < 2$, $m_{WH} > 0.5\,\text{TeV}$. The resulting SM cross sections from VBF, including the effect of the mixed Z/γ PDF, at 3 and 10 TeV MuC are

$$\sigma(\mu\bar{\mu} \to W^- H)^{3\text{TeV}}_{\text{VBF}} \approx 3.7 \text{ fb} , \qquad \sigma(\mu\bar{\mu} \to W^- H)^{10\text{TeV}}_{\text{VBF}} \approx 6.6 \text{ fb} . \tag{4.3}$$

On the other hand, the muon-neutrino-induced contribution are

$$\sigma(\mu\bar{\mu} \to W^- H)^{3\text{TeV}}_{\mu\bar{\nu}} \approx 0.16 \text{ fb} , \qquad \sigma(\mu\bar{\mu} \to W^- H)^{10\text{TeV}}_{\mu\bar{\nu}} \approx 0.031 \text{ fb} , \tag{4.4}$$

corresponding to a 4% and 0.5% effect at the two collider energies, respectively.

5 Conclusions

We have studied the neutrino content of a muon and the related phenomenology at a high energy muon collider. This specific aspect of EW PDFs falls into the broader topic of EW effects which become significant in the multi-TeV regime, offering new ways to test SM predictions in an unexplored energy range.

We reviewed how the neutrino PDF arises from the collinear emission of W bosons from the muon and provided an analytic approximate expression for the ν_μ PDF, which is in good agreement with the result derived from the numerical leading-logarithmic resummation of SM DGLAP equations by LePDF.

We identified two processes, electron plus neutrino and $W\gamma$ production, that are particularly sensitive to this neutrino PDF, providing potential experimental handles to isolate and test the theoretical predictions. Our results indicate that both processes can serve as theoretical laboratories for high-precision tests of the muon neutrino PDF. In case of electron plus neutrino production, we compared the results derived using the neutrino PDF with those obtained at leading-order from a Monte Carlo simulation. While our use of specific cuts in the fixed-order method was effective in isolating the collinear W emission and in bringing the two results in agreement, this contrasts with the inclusive nature of the PDF approach, which accounts for all potential collinear emissions. Achieving a more rigorous comparison would require consistent treatment across both methods, a goal that shows the need for further theoretical developments in handling electroweak radiation at high-energy muon colliders.

In the context of Higgs physics, we demonstrated that single-Higgs production at muon colliders is significantly influenced by both the muon and neutrino PDFs, with their effects being especially prominent at 10 TeV collider energies. These effects are relevant and much larger than the expected experimental precision. For example, for exclusive measurements where the final-state leptons are tagged, the cross section for the $\mu^+\mu^- H$ final state has a 3% contribution from the neutrino PDF, while the neutrino-induced $\mu\nu_\mu H$ final state has a cross section with size of about 25% of the $\mu\mu H$. In case of inclusive cross sections we find that at a 10 TeV MuC the muon and muon-neutrino PDFs affect the cross section due to ZZH-fusion by 8% and 27%, respectively, while the muon PDF modifies the WWH-fusion cross section by 3%. Accurate SM predictions for Higgs production will therefore require a careful treatment of these contributions to achieve the desired precision in measuring Higgs couplings.

Overall, our results underscore the importance of electroweak PDFs to provide accurate SM predictions for muon collider processes. Further studies are required to improve these PDFs with higher-order corrections and to implement them in event-generation tools, both of which could be instrumental to better understand the complementarity between the resummed and fixed-order approaches to treat EW radiation. Addressing these challenges will be critical for maximizing the potential of future muon collider experiments in exploring physics beyond the Standard Model.

Acknowledgments

DM thanks Davide Pagani for useful discussions. This manuscript has been authored by Fermi Research Alliance, LLC under Contract No. DE-AC02-07CH11359 with the U.S. Department of Energy, Office of High Energy Physics. DM acknowledges support by the Italian Ministry of University and Research (MUR) via the PRIN project n. 20224JR28W.

A Differential cross sections

For the production of two final state objects, assuming that the energy of the hard-scattering is much larger than the p_T of the initial-state collinear radiation and the masses of all objects, i.e. $p_T^{1,2},\ m_{1,2,3,4} \ll p_T^{3,4},\ \hat{s}$, then the triple-differential cross-section for the production of a final state X_3X_4 is given in terms of a convolution of the partonic cross section $d\hat{\sigma}/d\hat{t}$ with the initial-state PDFs:

$$\frac{d^3\sigma(\mu\bar{\mu}\to X_3X_4)}{dy_3dy_4dp_T} = \sum_{i,j} f_i^{\mu}\left(x_1,\frac{\hat{s}}{4}\right) f_j^{\bar{\mu}}\left(x_2,\frac{\hat{s}}{4}\right)\left(\frac{2p_T\hat{s}}{s_0}\right)\frac{d\hat{\sigma}}{d\hat{t}}(ij\to X_3X_4)(\hat{s},\hat{t})\ , \tag{A.1}$$

where s_0 is the collider center-of-mass energy squared, $\hat{s}$ and $\hat{t}$ are the partonic Mandelstam variables. All the kinematical variables can be expressed in terms of the two rapidities of the final-state particles, $y_{3,4}$, and their p_T (by conservation of transverse momentum $p_T \equiv p_{T,3} = p_{T,4}$):

$$\begin{aligned} y &\equiv \frac{y_3-y_4}{2}\ , \qquad Y \equiv \frac{y_3+y_4}{2}\ , \\ \hat{s} &= 4p_T^2\cosh^2 y\ , \qquad \hat{t} = -2p_T^2 e^{-y}\cosh y\ , \\ x_1 &= \frac{2p_T\cosh y}{\sqrt{s_0}}e^{Y}\ , \qquad x_2 = \frac{2p_T\cosh y}{\sqrt{s_0}}e^{-Y}\ . \end{aligned} \tag{A.2}$$

Being $x_{1,2} \le 1$, the kinematic constraints on pT, y_3 and y_4 are

$$p_T \le \frac{\sqrt{s_0}}{2}\frac{e^{\pm Y}}{\cosh y}. \tag{A.3}$$

Fixing y_3, the two functions at the RHS of Eq. (A.3) intersect at $(y_4, p_T) = (-y_3, \sqrt{s_0}/2\cosh y_3)$. Then after integration on y_4 the following region is kinematically forbidden $\forall(y_3; p_T)$:

$$p_T > \frac{\sqrt{s_0}}{2\cosh y_3}. \tag{A.4}$$

Parton luminosities

A useful quantity that can be derived from PDFs are the parton luminosities, that describe the probability of having a certain pair of partons (one from each of the two colliding beams) with a given partonic invariant mass $\sqrt{\hat{s}}$, if the total invariant mass of the collision is $\sqrt{s_0}$. They are obtained as:

$$\mathcal{L}_{ij}(\hat{s}, s_0) = \int_0^1 \frac{dz}{z} f_{i;\mu}\left(z, \frac{\hat{s}}{4}\right) f_{j;\bar{\mu}}\left(\frac{\hat{s}}{z s_0}, \frac{\hat{s}}{4}\right) \ . \tag{A.5}$$

Using parton luminosities, a total cross section for the production of a given hard final state Y, inclusive over collinear radiation X, can be computed simply by convoluting them with the partonic cross section:

$$\frac{d\sigma}{d\sqrt{\hat{s}}}(\mu\bar{\mu} \to Y + X) = \sum_{i,j} \frac{2\sqrt{\hat{s}}}{s_0} \mathcal{L}_{ij}(\hat{s}, s_0) \hat{\sigma}(ij \to Y)(\hat{s}) \ . \tag{A.6}$$

Depending on the situation it can be useful to derive the total cross section without using the parton luminosities but putting explicitly the PDFs:

$$\sigma(\mu\bar{\mu} \to Y + X)(s_0) = \sum_{i,j} \int_0^1 dx_1 \int_0^1 dx_2 \, f_i\left(x_1, \hat{s}/4\right) \bar{f}_j\left(x_2, \hat{s}/4\right) \hat{\sigma}(ij \to Y)(\hat{s}), \tag{A.7}$$

where the CoM energy of the interacting partons is given by $\hat{s} = x_1 x_2 s_0$.

B Unpolarized single-Higgs production

Using the PDF approach, single-Higgs production can occur through various channels, some of which were not included in Table 1. In that table, we only reported channels with significantly large cross sections. Those results were obtained by convoluting polarized partonic cross sections with the corresponding PDFs, as discussed in Section 2. To estimate the magnitude of the contributions omitted in Table 1, we now compute the total cross sections for the process $\mu(\ell_1)\bar{\mu}(\ell_2) \to \ell_3\ell_4 H$, where $\mu(\bar{\mu})$ represents the muon (anti-muon) beams, ℓ_1 and ℓ_2 are the partons participating in the interaction from within μ and $\bar{\mu}$, and ℓ_3 and ℓ_4 are the final-state leptons. For simplicity, we compute unpolarized partonic cross sections and convolute them with the PDFs summed over different helicities. We present the total cross section by using the PDFs for processes involving $\ell_1, \ell_2 = \mu^-, \mu^+, \nu_\mu, \bar{\nu}_\mu$, considering scenarios at both a 3 TeV and a 10 TeV MuC. The results for all partonic subprocesses are shown in Table 3, where we do not report charge-conjugate processes which have identical cross sections as the listed ones.

$\mu\bar{\mu} \to \nu_\mu\bar{\nu}_\mu H$	3 TeV MuC	10 TeV MuC
Initial partons	σ [fb]	σ [fb]
$\mu(\mu^-)\bar{\mu}(\mu^+)$	463	767
$\mu(\nu_\mu)\bar{\mu}(\bar{\nu}_\mu)$	7.8×10^{-2}	1.01
$\mu(\mu^+)\bar{\mu}(\mu^-)$	1.2×10^{-5}	1.0×10^{-4}
$\mu(\bar{\nu}_\mu)\bar{\mu}(\nu_\mu)$	4.1×10^{-8}	1.1×10^{-6}
$\mu\bar{\mu} \to \mu^+\mu^- H$	3 TeV MuC	10 TeV MuC
Initial partons	σ [fb]	σ [fb]
$\mu(\mu^-)\bar{\mu}(\mu^+)$	48.27	81.05
$\mu(\nu_\mu)\bar{\mu}(\bar{\nu}_\mu)$	1.9×10^{-1}	2.42
$\mu(\mu^+)\bar{\mu}(\mu^-)$	1.2×10^{-6}	1.4×10^{-5}
$\mu(\bar{\nu}_\mu)\bar{\mu}(\nu_\mu)$	1.0×10^{-7}	2.7×10^{-6}
$\mu\bar{\mu} \to \mu^-\bar{\nu}_\mu H$	3 TeV MuC	10 TeV MuC
Initial partons	σ [fb]	σ [fb]
$\mu(\mu^-)\bar{\mu}(\bar{\nu}_\mu)$	2.44	10.2
$\mu(\bar{\nu}_\mu)\bar{\mu}(\mu^-)$	3.5×10^{-7}	3.6×10^{-6}
Parton process	3 TeV MuC	10 TeV MuC
	σ [fb]	σ [fb]
$\mu(\mu^-)\bar{\mu}(\nu_\mu) \to \mu^-\nu_\mu H$	2.5×10^{-2}	1.7×10^{-1}
$\mu(\mu^-)\bar{\mu}(\mu^-) \to \mu^-\mu^- H$	1.1×10^{-2}	4.6×10^{-2}
$\mu(\nu_\mu)\bar{\mu}(\mu^-) \to \nu_\mu\mu^- H$	1.7×10^{-3}	1.8×10^{-2}
$\mu(\nu_\mu)\bar{\mu}(\nu_\mu) \to \nu_\mu\nu_\mu H$	3.6×10^{-6}	7.3×10^{-5}

Table 3. Cross sections for all partonic single-Higgs production processes, after incorporating lepton PDFs and in the unpolarized approximation, for a 3 and 10 TeV MuC. The initial state partons are given in the left column. The cross sections (σ) are evaluated at a factorization scale of $\mu_F = \sqrt{\hat{s}}/2$.

References

[1] K. Long, D. Lucchesi, M. Palmer, N. Pastrone, D. Schulte and V. Shiltsev, *Muon colliders to expand frontiers of particle physics*, *Nature Phys.* **17** (2021) 289–292, [2007.15684].

[2] H. Al Ali et al., *The muon Smasher's guide*, *Rept. Prog. Phys.* **85** (2022) 084201, [2103.14043].

[3] C. Aime et al., *Muon Collider Physics Summary*, 2203.07256.

[4] K. M. Black et al., *Muon Collider Forum report*, *JINST* **19** (2024) T02015, [2209.01318].

[5] C. Accettura et al., *Towards a muon collider*, *Eur. Phys. J. C* **83** (2023) 864, [2303.08533]. [Erratum: Eur.Phys.J.C 84, 36 (2024)].

[6] P. Andreetto et al., *Higgs Physics at a $\sqrt{s} = 3$ TeV Muon Collider with detailed detector simulation*, 2405.19314.

[7] C. Accettura et al., *Interim report for the International Muon Collider Collaboration (IMCC)*, 2407.12450.

[8] T. Han, D. Liu, I. Low and X. Wang, *Electroweak couplings of the Higgs boson at a multi-TeV muon collider*, *Phys. Rev. D* **103** (2021) 013002, [2008.12204].

[9] M. Forslund and P. Meade, *High precision higgs from high energy muon colliders*, *JHEP* **08** (2022) 185, [2203.09425].

[10] M. Ruhdorfer, E. Salvioni and A. Wulzer, *Invisible Higgs boson decay from forward muons at a muon collider*, *Phys. Rev. D* **107** (2023) 095038, [2303.14202].

[11] M. Forslund and P. Meade, *Precision Higgs width and couplings with a high energy muon collider*, *JHEP* **01** (2024) 182, [2308.02633].

[12] P. Andreetto et al., *Higgs Physics at a $\sqrt{s} = 3$ TeV Muon Collider with detailed detector simulation*, 2405.19314.

[13] P. Li, Z. Liu and K.-F. Lyu, *Higgs boson width and couplings at high energy muon colliders with forward muon detection*, *Phys. Rev. D* **109** (2024) 073009, [2401.08756].

[14] T. Han, Z. Liu, L.-T. Wang and X. Wang, *WIMPs at High Energy Muon Colliders*, *Phys. Rev. D* **103** (2021) 075004, [2009.11287].

[15] D. Buttazzo, R. Franceschini and A. Wulzer, *Two Paths Towards Precision at a Very High Energy Lepton Collider*, *JHEP* **05** (2021) 219, [2012.11555].

[16] R. Capdevilla, F. Meloni, R. Simoniello and J. Zurita, *Hunting wino and higgsino dark matter at the muon collider with disappearing tracks*, *JHEP* **06** (2021) 133, [2102.11292].

[17] S. Bottaro, D. Buttazzo, M. Costa, R. Franceschini, P. Panci, D. Redigolo et al., *Closing the window on WIMP Dark Matter*, *Eur. Phys. J. C* **82** (2022) 31, [2107.09688].

[18] S. Chen, A. Glioti, R. Rattazzi, L. Ricci and A. Wulzer, *Learning from radiation at a very high energy lepton collider*, *JHEP* **05** (2022) 180, [2202.10509].

[19] S. Bottaro, D. Buttazzo, M. Costa, R. Franceschini, P. Panci, D. Redigolo et al., *The last complex WIMPs standing*, *Eur. Phys. J. C* **82** (2022) 992, [2205.04486].

[20] A. Azatov, F. Garosi, A. Greljo, D. Marzocca, J. Salko and S. Trifinopoulos, *New physics in $b \to s\mu\mu$: FCC-hh or a muon collider?*, *JHEP* **10** (2022) 149, [2205.13552].

[21] D. Liu, L.-T. Wang and K.-P. Xie, *Composite resonances at a 10 TeV muon collider*, *JHEP* **04** (2024) 084, [2312.09117].

[22] K. Korshynska, M. Löschner, M. Marinichenko, K. Mękała and J. Reuter, *Z' boson mass reach and model discrimination at muon colliders*, *Eur. Phys. J. C* **84** (2024) 568, [2402.18460].

[23] R. Capdevilla, F. Meloni and J. Zurita, *Discovering Electroweak Interacting Dark Matter at Muon Colliders using Soft Tracks*, 2405.08858.

[24] D. Amati, A. Bassetto, M. Ciafaloni, G. Marchesini and G. Veneziano, *A Treatment of Hard Processes Sensitive to the Infrared Structure of QCD*, *Nucl. Phys. B* **173** (1980) 429–455.

[25] P. Ciafaloni and D. Comelli, *Sudakov enhancement of electroweak corrections*, *Phys. Lett. B* **446** (1999) 278–284, [hep-ph/9809321].

[26] M. Ciafaloni, P. Ciafaloni and D. Comelli, *Electroweak double logarithms in inclusive observables for a generic initial state*, *Phys. Lett. B* **501** (2001) 216–222, [hep-ph/0007096].

[27] M. Ciafaloni, P. Ciafaloni and D. Comelli, *Bloch-Nordsieck violating electroweak corrections to inclusive TeV scale hard processes*, *Phys. Rev. Lett.* **84** (2000) 4810–4813, [hep-ph/0001142].

[28] M. Ciafaloni, P. Ciafaloni and D. Comelli, *Electroweak Bloch-Nordsieck violation at the TeV scale: 'Strong' weak interactions?*, *Nucl. Phys. B* **589** (2000) 359–380, [hep-ph/0004071].

[29] M. Ciafaloni, P. Ciafaloni and D. Comelli, *Bloch-Nordsieck violation in spontaneously broken Abelian theories*, *Phys. Rev. Lett.* **87** (2001) 211802, [hep-ph/0103315].

[30] A. V. Manohar and W. J. Waalewijn, *Electroweak Logarithms in Inclusive Cross Sections*, *JHEP* **08** (2018) 137, [1802.08687].

[31] J. Chen, T. Han and B. Tweedie, *Electroweak Splitting Functions and High Energy Showering*, *JHEP* **11** (2017) 093, [1611.00788].

[32] S. Dawson, *The Effective W Approximation*, *Nucl. Phys. B* **249** (1985) 42–60.

[33] G. L. Kane, W. W. Repko and W. B. Rolnick, *The Effective W+-, Z0 Approximation for High-Energy Collisions*, *Phys. Lett. B* **148** (1984) 367–372.

[34] M. Ciafaloni, P. Ciafaloni and D. Comelli, *Towards collinear evolution equations in electroweak theory*, *Phys. Rev. Lett.* **88** (2002) 102001, [hep-ph/0111109].

[35] P. Ciafaloni and D. Comelli, *Electroweak evolution equations*, *JHEP* **11** (2005) 022, [hep-ph/0505047].

[36] C. W. Bauer, N. Ferland and B. R. Webber, *Standard Model Parton Distributions at Very High Energies*, *JHEP* **08** (2017) 036, [1703.08562].

[37] C. W. Bauer, N. Ferland and B. R. Webber, *Combining initial-state resummation with fixed-order calculations of electroweak corrections*, *JHEP* **04** (2018) 125, [1712.07147].

[38] C. W. Bauer and B. R. Webber, *Polarization Effects in Standard Model Parton Distributions at Very High Energies*, *JHEP* **03** (2019) 013, [1808.08831].

[39] T. Han, Y. Ma and K. Xie, *High energy leptonic collisions and electroweak parton distribution functions*, *Phys. Rev. D* **103** (2021) L031301, [2007.14300].

[40] T. Han, Y. Ma and K. Xie, *Quark and gluon contents of a lepton at high energies*, *JHEP* **02** (2022) 154, [2103.09844].

[41] F. Garosi, D. Marzocca and S. Trifinopoulos, *LePDF: Standard Model PDFs for high-energy lepton colliders*, *JHEP* **09** (2023) 107, [2303.16964].

[42] P. Ciafaloni, G. Co', D. Colferai and D. Comelli, *Electroweak evolution equations and isospin conservation*, *JHEP* **07** (2024) 237, [2403.08583].

[43] E. Fermi, *On the Theory of the impact between atoms and electrically charged particles*, *Z. Phys.* **29** (1924) 315–327.

[44] L. D. Landau and E. M. Lifschitz, *ON THE PRODUCTION OF ELECTRONS AND POSITRONS BY A COLLISION OF TWO PARTICLES*, *Phys. Z. Sowjetunion* **6** (1934) 244.

[45] C. F. von Weizsacker, *Radiation emitted in collisions of very fast electrons*, *Z. Phys.* **88** (1934) 612–625.

[46] E. J. Williams, *Nature of the high-energy particles of penetrating radiation and status of ionization and radiation formulae*, *Phys. Rev.* **45** (1934) 729–730.

[47] A. Costantini, F. De Lillo, F. Maltoni, L. Mantani, O. Mattelaer, R. Ruiz et al., *Vector boson fusion at multi-TeV muon colliders*, *JHEP* **09** (2020) 080, [2005.10289].

[48] R. Ruiz, A. Costantini, F. Maltoni and O. Mattelaer, *The Effective Vector Boson Approximation in high-energy muon collisions*, *JHEP* **06** (2022) 114, [2111.02442].

[49] Z. Kunszt and D. E. Soper, *On the Validity of the Effective W Approximation*, *Nucl. Phys. B* **296** (1988) 253–289.

[50] P. Borel, R. Franceschini, R. Rattazzi and A. Wulzer, *Probing the Scattering of Equivalent Electroweak Bosons*, *JHEP* **06** (2012) 122, [1202.1904].

[51] G. Cuomo, L. Vecchi and A. Wulzer, *Goldstone Equivalence and High Energy Electroweak Physics*, *SciPost Phys.* **8** (2020) 078, [1911.12366].

[52] V. N. Gribov and L. N. Lipatov, *Deep inelastic e p scattering in perturbation theory*, *Sov. J. Nucl. Phys.* **15** (1972) 438–450.

[53] Y. L. Dokshitzer, *Calculation of the Structure Functions for Deep Inelastic Scattering and e+ e- Annihilation by Perturbation Theory in Quantum Chromodynamics.*, *Sov. Phys. JETP* **46** (1977) 641–653.

[54] G. Altarelli and G. Parisi, *Asymptotic Freedom in Parton Language*, *Nucl. Phys. B* **126** (1977) 298–318.

[55] F. Bloch and A. Nordsieck, *Note on the Radiation Field of the electron*, *Phys. Rev.* **52** (1937) 54–59.

[56] D. Marzocca and A. Stanzione, *On the impact of the mixed Z/γ PDF at muon colliders*, 2408.13191.

[57] V. Di Benedetto, C. Gatto, A. Mazzacane, N. V. Mokhov, S. I. Striganov and N. K. Terentiev, *A Study of Muon Collider Background Rejection Criteria in Silicon Vertex and Tracker Detectors*, *JINST* **13** (2018) P09004, [1807.00074].

[58] N. V. Mokhov and S. I. Striganov, *Detector Background at Muon Colliders*, *Phys. Procedia* **37** (2012) 2015–2022, [1204.6721].

[59] R. W. Brown, D. Sahdev and K. O. Mikaelian, *W+- Z0 and W+- gamma Pair Production in Neutrino e, p p, and anti-p p Collisions*, *Phys. Rev. D* **20** (1979) 1164.

[60] U. Baur, S. Errede and G. L. Landsberg, *Rapidity correlations in $W\gamma$ production at hadron colliders*, *Phys. Rev. D* **50** (1994) 1917–1930, [hep-ph/9402282].

[61] U. Baur, T. Han and J. Ohnemus, *Amplitude zeros in W+- Z production*, *Phys. Rev. Lett.* **72** (1994) 3941–3944, [hep-ph/9403248].

[62] K. O. Mikaelian, M. A. Samuel and D. Sahdev, *The Magnetic Moment of Weak Bosons Produced in p p and p anti-p Collisions*, *Phys. Rev. Lett.* **43** (1979) 746.

[63] D0 collaboration, V. M. Abazov et al., *First study of the radiation-amplitude zero in $W\gamma$ production and limits on anomalous $WW\gamma$ couplings at $\sqrt{s}$ = 1.96- TeV*, *Phys. Rev. Lett.* **100** (2008) 241805, [0803.0030].

[64] CMS collaboration, S. Chatrchyan et al., *Measurement of the $W\gamma$ and $Z\gamma$ Inclusive Cross Sections in pp Collisions at $\sqrt{s} = 7$ TeV and Limits on Anomalous Triple Gauge Boson Couplings*, *Phys. Rev. D* **89** (2014) 092005, [1308.6832].

[65] CMS collaboration, A. Tumasyan et al., *Measurement of $W^{\pm}\gamma$ differential cross sections in proton-proton collisions at $\sqrt{s}$ = 13 TeV and effective field theory constraints*, *Phys. Rev. D* **105** (2022) 052003, [2111.13948].

[66] ATLAS collaboration, G. Aad et al., *Studies of the Energy Dependence of Diboson Polarization Fractions and the Radiation-Amplitude-Zero Effect in WZ Production with the ATLAS Detector*, *Phys. Rev. Lett.* **133** (2024) 101802, [2402.16365].

[67] ATLAS collaboration, M. Aaboud et al., *Measurement of $W^{\pm}Z$ production cross sections and*

gauge boson polarisation in pp collisions at $\sqrt{s} = 13$ *TeV with the ATLAS detector*, *Eur. Phys. J. C* **79** (2019) 535, [1902.05759].

[68] R. M. Capdevilla, R. Harnik and A. Martin, *The radiation valley and exotic resonances in* $W\gamma$ *production at the LHC*, *JHEP* **03** (2020) 117, [1912.08234].

[69] R. Capdevilla and T. Han, *In preparation (2024)*, .

[70] Y. Ma, D. Pagani and M. Zaro, *EW corrections and Heavy Boson Radiation at a high-energy muon collider*, 2409.09129.

[71] J. Alwall, R. Frederix, S. Frixione, V. Hirschi, F. Maltoni, O. Mattelaer et al., *The automated computation of tree-level and next-to-leading order differential cross sections, and their matching to parton shower simulations*, *JHEP* **07** (2014) 079, [1405.0301].

[72] M. Narain et al., *The Future of US Particle Physics - The Snowmass 2021 Energy Frontier Report*, 2211.11084.